

# A comparison of explosion energies for simulated and observed core-collapse supernovae

Jeremiah W. Murphy,<sup>1★</sup> Quintin Mabanta<sup>1</sup> and Joshua C. Dolence<sup>2</sup>

<sup>1</sup>*Department of Physics, Florida State University, 77 Chieftan Way, Tallahassee, FL 32306, USA*

<sup>2</sup>*Los Alamos National Laboratory, 87545-1362, Los Alamos, NM*

Accepted 2019 July 29. Received 2019 July 24; in original form 2019 April 20

## ABSTRACT

There are now 20 multidimensional core-collapse supernova (CCSN) simulations that explode. However, these simulations have explosion energies that are a few times  $10^{50}$  erg, not  $10^{51}$  erg. In this manuscript, we compare the inferred explosion energies of these simulations and observations of 40 SN IIP. Assuming a lognormal distribution, the mean explosion energy for these observations is  $\mu_{\text{obs}} = -0.23^{+0.08}_{-0.12} (\log_{10}(E/10^{51} \text{ erg}))$  and the width is  $\sigma_{\text{obs}} = 0.52^{+0.09}_{-0.08}$ . Only three CCSN codes have sufficient simulations to compare with observations: CHIMERA, CoCoNuT-FMT, and FORNAX. Currently, FORNAX has the largest sample of simulations. The two-dimensional FORNAX simulations show a correlation between explosion energy and progenitor mass, ranging from linear to quadratic,  $E_{\text{sim}} \propto M^{1-2}$ ; this correlation is consistent with inferences from observations. In addition, we infer the ratio of the observed-to-simulated explosion energies,  $\Delta = \log_{10}(E_{\text{obs}}/E_{\text{sim}})$ . For the CHIMERA set,  $\Delta = 0.25 \pm 0.07$ ; for CoCoNuT-FMT,  $\Delta = 0.49 \pm 0.07$ ; for FORNAX2D,  $\Delta = 0.62 \pm 0.06$ , and for FORNAX3D,  $\Delta = 0.85 \pm 0.07$ . On average, the simulations are less energetic than inferred energies from observations ( $\Delta \approx 0.6$ ), but we also note that the variation among the simulations [ $\max(\Delta) - \min(\Delta) \approx 0.6$ ] is as large as this average offset. This suggests that further improvements to the simulations could resolve the discrepancy. Furthermore, both the simulations and observations are heavily biased. In this preliminary comparison, we model these biases, but to more reliably compare the explosion energies, we recommend strategies to unbiased both the simulations and observations.

**Key words:** methods: statistical – stars: massive – supernovae: general.

## 1 INTRODUCTION

A primary goal of core-collapse supernovae theory is to predict which stars will explode, but for more than two decades, the more pressing challenge has been to produce at least one successful explosion in numerical simulations. Recent multidimensional simulations are finally producing self-consistent explosions (Lentz et al. 2015; Melson, Janka & Marek 2015a; Müller 2015; Bruenn et al. 2016; Summa et al. 2016; Radice et al. 2017; O’Connor & Couch 2018; Ott et al. 2018; Vartanyan et al. 2018; Burrows, Radice & Vartanyan 2019; Müller et al. 2019; Vartanyan et al. 2019). While there are still only a handful of simulations with successful explosions, a trend is already emerging; the explosion energies of simulations tend to be less energetic than explosion energies inferred from observations. In this manuscript, we quantify the discrepancy between simulations and observations.

Over the last several decades, CCSN simulations have become much more computationally expensive (requiring 10s of millions of CPU-hours) but they also seem to be converging towards successful explosions. Colgate & White (1966) was the first to suggest that the change in gravitational energy due to core collapse could power the supernova explosion; they also suggested that neutrinos transfer this energy from the core to the mantle. However, more detailed modelling indicates that the bounce shock quickly stalls into an accretion shock due to electron capture and neutrino losses but mostly due to nuclear disassociation (Hillebrandt & Mueller 1981; Mazurek 1982). Using one-dimensional neutrino radiation hydrodynamic simulations, Wilson (1985) and Bethe & Wilson (1985) suggested that neutrinos eventually relaunch the stalled shock into an explosion. However, most modern one-dimensional simulations do not explode. During the 1990s, two-dimensional simulations using gray flux-limited diffusion hinted that convection might aide the explosion when one-dimensional simulations failed (Benz, Colgate & Herant 1994; Herant et al. 1994; Burrows, Hayes & Fryxell 1995; Janka & Müller 1995). Murphy & Burrows

\* E-mail: [jwmurphy@fsu.edu](mailto:jwmurphy@fsu.edu)

(2008) investigated the conditions for explosion and found that the neutrino luminosity required for explosion is 30 per cent less in two-dimensional than one-dimensional. Mabanta & Murphy (2018) derived the conditions for explosion with and without a convection model. They found that the convection model does reduce the explosion condition by 30 per cent in agreement with simulations, and they found that a large part of the reduction is caused by turbulent dissipation.

These investigations suggest a minimum set of requirements for self-consistent core-collapse supernova simulations. General relativity (GR) is likely important, so the code should employ GR or at least a post Newtonian potential inspired by GR. Neutrino transport should include the interactions for electron, mu, and tau flavours, and it should be multi-angle and multi-energy. Finally, the simulations should be multidimensional, preferably three-dimensional, but two-dimensional simulations have shown similar explosion conditions (Hanke et al. 2012) and energetics (Burrows et al. 2019). Following is a list of publications that report explosive simulations using codes with these minimum requirements: Lentz et al. (2015), Müller (2015), Bruenn et al. (2016), Melson et al. (2015a), Summa et al. (2016), Radice et al. (2017), O'Connor & Couch (2018), Ott et al. (2018), Vartanyan et al. (2018), Müller et al. (2019), Vartanyan et al. (2019), and Burrows et al. (2019). Of these, the following publications report positive explosion energies that begin to plateau in energy: Müller (2015), Bruenn et al. (2016), Melson et al. (2015a), Radice et al. (2017), Vartanyan et al. (2018), Müller et al. (2019), Vartanyan et al. (2019), and Burrows et al. (2019). In general, the explosion energies reported range from 0.1 to  $0.9 \times 10^{51}$  erg.

Arnett (1980) suggested that one may infer explosion energies of observed type IIP SNe (SN IIP) by modelling the light curve and spectra of SN IIP. In general, the light-curve shape depends upon four parameters: the explosion energy, ejecta mass, nickel mass, and progenitor radius (Popov 1993; Kasen & Woosley 2009; Dessart & Hillier 2019; Goldberg, Bildsten & Paxton 2019). On the other hand, the light-curve shape of SN IIP is most readily described by three parameters: the brightness during the plateau phase (usually at 50 d), the duration of the plateau, and the brightness during the co-decay tail. The latter constrains the nickel mass. To close the system of equations, investigators had assumed that measuring the velocity during the plateau phase (at 50 d) could close the system giving a unique solution (Pejcha & Prieto 2015). Under this assumption, this investigation infers explosion energies for SN IIP that range from  $0.5$  to  $4.0 \times 10^{51}$  erg. However, Dessart & Hillier (2019) and Goldberg et al. (2019) note significant degeneracies; in particular, Goldberg et al. (2019) emphasize that the observed correlation between luminosity and velocity (Hamuy & Pinto 2002) precludes using velocity as an extra constraint. Therefore, Goldberg et al. (2019) recommend that another constraint for the progenitor radius is required.

While there are few constraints on progenitor radii for observed SN IIP, there are constraints on red supergiant (RSG) radii, the progenitors of SN IIP. Fortunately, the distribution of radii for RSGs is relatively narrow and provides a strong prior on the radii for the SN IIP progenitors. Davies, Crowther & Beasor (2018) compile the brightness and effective temperature of 581 RSGs in LMC and SMC. The mean inferred radius of these RSGs is  $500 R_{\odot}$ , and most RSGs have radii that are within a factor of 2 of this mean. In this manuscript, we use this prior and infer the explosion energy of SN IIP.

In this manuscript, we infer the observed explosion energies for 40 SN IIP and perform a preliminary comparison with multidimensional simulations.

In Section 2, we discuss the observations, use the observed distribution of RSG radii as a prior and infer the explosion energies from observations. In Section 3, we describe the sample of multidimensional simulations. All of the simulations show a trend towards an asymptotic explosion energy, but only a few actually reach an asymptotic explosion energy. Therefore, in Section 4, we propose a model for the asymptotic explosion energy and infer an extrapolated explosion energy for each simulation. Each set of simulations does not yet sample the full range of progenitors that lead to SN IIP. Therefore, in Section 5, we assume a model correlating explosion energy and progenitor mass, infer the parameters of this model, and use the results to infer the full distribution of simulation explosion energies. Then, we compare the simulations and observations in Section 6 and infer the discrepancy between them. Finally, in Section 7, we summarize and discuss how to improve the inference by addressing biases in both simulations and observations.

## 2 INFERRED EXPLOSION ENERGIES FROM OBSERVATIONS

To infer the explosion energies from observations, we use the fitting formula, equation (22), of Goldberg et al. (2019):

$$E_{\text{exp}} = -0.728 + 2.148 \log(L_{42}) - 0.280 \log(M_{\text{Ni}}) + 2.091 \log(t_{p,2}) - 1.632 \log(R_{500}), \quad (1)$$

where  $L_{42}$  is the plateau luminosity at day 50 in units of  $10^{42}$  erg  $\text{s}^{-1}$ ,  $M_{\text{Ni}}$  is the nickel mass in  $M_{\odot}$ ,  $t_{p,2}$  is the duration of the plateau in units of 100 d, and  $R_{500}$  is the progenitor radius in units of  $500 R_{\odot}$ . For the light-curve parameters ( $L_{42}$ ,  $M_{\text{Ni}}$ , and  $t_{p,2}$ ), we consider two sources: Pejcha & Prieto (2015) and Müller et al. (2017b); these two sources include 40 ‘nearby and well observed’ SN IIP. Unfortunately, there are no progenitor radius constraints for the entire set of SNe. To constrain the progenitor radii, we use the radius distribution for RSGs as a prior.

In addition to reporting the light-curve parameters for 40 SN IIP, Pejcha & Prieto (2015) and Müller et al. (2017b) also use Bayesian inference to infer the explosion parameters, their associated uncertainties, and covariances. These works represent the most thorough analysis of the uncertainty and covariances for the explosion parameters. However, since they assumed that the velocity at 50 d would provide an additional constraint, we are unable to use their inferred explosion parameters and uncertainties. Instead, we use their light-curve parameters and equation (1) to infer the explosion energy. Instead of calculating the full covariance matrix as in Pejcha & Prieto (2015), we simply assume Gaussian, uncorrelated errors and the standard error propagation.

To calculate the radii for RSGs, we use the luminosity and effective temperature,  $T_{\text{eff}}$ , of RSGs. Fig. 1 shows the Hertzsprung–Russell (HR) diagram for cool, luminous stars in the Large and Small Magellanic Clouds (LMC and SMC) (Davies et al. 2018). The clump of stars near 4000 K are the RSGs. In general, the RSGs for the LMC are cooler than the RSGs in the SMC; in particular, the SMC RSGs have  $T_{\text{eff}} < 4300$  K, and the LMC RSGs have  $T_{\text{eff}} < 4000$  K. These temperatures correspond to spectral types later than G7 for the SMC and K3 for the LMC. Using these  $T_{\text{eff}}$  cuts, there are 303 RSGs in SMC sample, and there are 278 RSGs in the LMC sample for a total of 581 RSGs in the combined sample. It is likely that the latest types are the progenitors of SN IIP (Davies & Beasor 2018); While the red colours of SN IIP progenitors are consistent with this statement (Smartt 2015), the spectral types have yet to

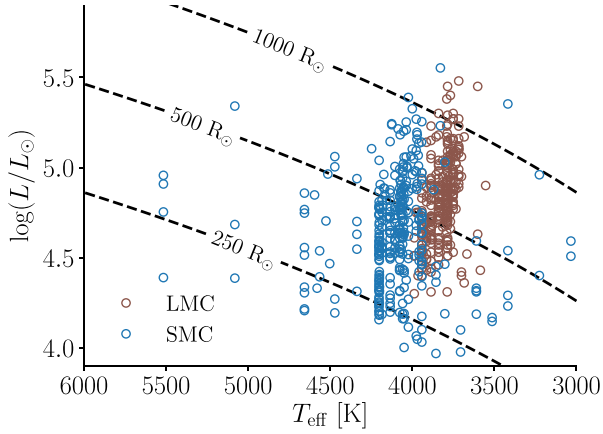


**Figure 1.** The HR diagram for cool, luminous stars in the LMC and the SMC (Davies et al. 2018). The clump of stars near 4000 K are red supergiants (RSGs). The typical radius for the RSGs is  $500 R_{\odot}$ , and the full range of radii differs only by a factor of 4 (between  $250 R_{\odot}$  and  $1000 R_{\odot}$ ). SMC RSGs have effective temperatures,  $T_{\text{eff}}$ , less than 4300 K, and the LMC RSGs have  $T_{\text{eff}} < 4000$  K.

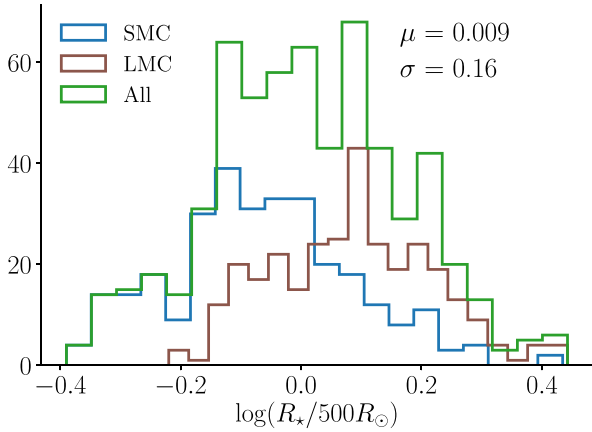


**Figure 2.** The radii for RSGs in LMC and SMC. On average, the SMC radii are smaller than the LMC radii by about 0.2 dex. For the entire population, the mean RSG radius is  $\mu = 0.009$  in units of  $\log_{10}(R/500 R_{\odot})$ , and the standard deviation is  $\sigma = 0.16$ . We use the combined distribution as a prior in equation (1) when inferring the explosion energies of the 40 observed SNe (Pejcha & Prieto 2015; Müller et al. 2017b).

be confirmed with observations. To construct the most conservative prior for RSG radii, we consider all RSGs in both samples.

Fig. 2 shows the distributions of radii for the RSGs in the LMC, SMC, and both. The distributions are log normal; the mean for all is  $\mu = 0.009$  [in units of  $\log_{10}(R/500 R_{\odot})$ ], and the standard deviation is  $\sigma = 0.16$ . The mean for the SMC is around  $-0.1$ , while the mean for the LMC is  $0.1$ . This systematic difference in radii has an impact on the inferred explosion energies via equation (1). Using the SMC distribution as a prior would lead to explosion energies that are 0.3 dex larger compared to using the LMC distribution. To account for both this systematic offset and the intrinsic variation in radii, we use the combined distribution to represent the prior for RSG radii. Using this distribution as a prior, we then use light-curve parameters from Pejcha & Prieto (2015) and Müller et al. (2017b), and equation (1) from Goldberg et al. (2019) to infer the explosion energies and uncertainties. The inferred explosion energies and uncertainties are in Table 1.

**Table 1.** Explosion energies inferred from SN IIP observations.  $\epsilon$  is the mode, and  $\sigma_{\epsilon}$  is the uncertainty. The light-curve data is from Pejcha & Prieto (2015) and Müller et al. (2017b); for the progenitor radii, we use the RSG distribution as a prior (Fig. 2), and we use the fitting formula from Goldberg et al. (2019), equation (1).

Name	$\epsilon = \log_{10}(E_{\text{obs}}/10^{51})$	$\sigma_{\epsilon}$
SN 1980K	-1.54	0.31
SN 1992H	1.05	0.33
SN 1995ad	0.81	0.37
SN 1996W	0.11	0.34
SN 1999em	-0.07	0.31
SN 2001dc	-1.80	0.34
SN 2002hh	-0.26	0.32
SN 2004A	-0.32	0.31
SN 2004dj	-0.69	0.32
SN 2004et	-0.04	0.31
SN 2005cs	-0.87	0.32
SN 2006bp	0.30	0.31
SN 2007od	1.37	0.31
SN 2008bk	-0.68	0.53
SN 2008in	-0.26	0.64
SN 2009bw	0.04	0.30
SN 2009dd	-0.58	0.40
SN 2009js	-0.57	0.38
SN 2009N	-0.49	0.31
SN 2012A	-0.67	0.30
SN 2012aw	0.34	0.30
SN 1992ba	-0.16	0.48
SN 2002gw	-0.12	0.39
SN 2003B	-0.55	0.59
SN 2003bn	-0.28	0.35
SN 2003E	-0.20	0.40
SN 2003ef	0.27	0.39
SN 2003fb	-0.50	0.43
SN 2003hd	-0.26	0.35
SN 2003hn	-0.64	0.36
SN 2003ho	-1.09	0.34
SN 2003T	-0.48	0.33
SN 2009ib	-0.42	0.33
SN 2012ec	-0.23	0.31
SN 2013ab	0.11	0.43
SN 2013ej	-0.43	0.35
SN 2013fs	-0.35	0.33
SN 2014G	-0.50	0.34
ASSASSN-14gm	-0.06	0.35
ASSASSN-14ha	-0.53	0.38

Next, we infer the distribution of observed explosion energies by modelling the mean ( $\mu_{\text{obs}}$ ) and width ( $\sigma_{\text{obs}}$ ) of the observations. For a rough estimate, one may calculate the mean and variance of the modes (second column in Table 1). However, when the uncertainties in the observations are large, these estimates can easily be biased. In particular, the observed variance in the distribution is a convolution of the true width and the large uncertainties, so simply calculating the variance of the observations will lead to an over estimation of the width. Therefore, we use Bayesian inference to infer the distribution of explosion energies.

The posterior distribution is

$$P(\mu_{\text{obs}}, \sigma_{\text{obs}} | \{\epsilon_i, \sigma_{\epsilon_i}\})$$

$$\propto \prod_i \mathcal{L}(\epsilon_i | \sigma_{\epsilon_i}, \mu_{\text{obs}}, \sigma_{\text{obs}}) P(\mu_{\text{obs}}) P(\sigma_{\text{obs}}), \quad (2)$$

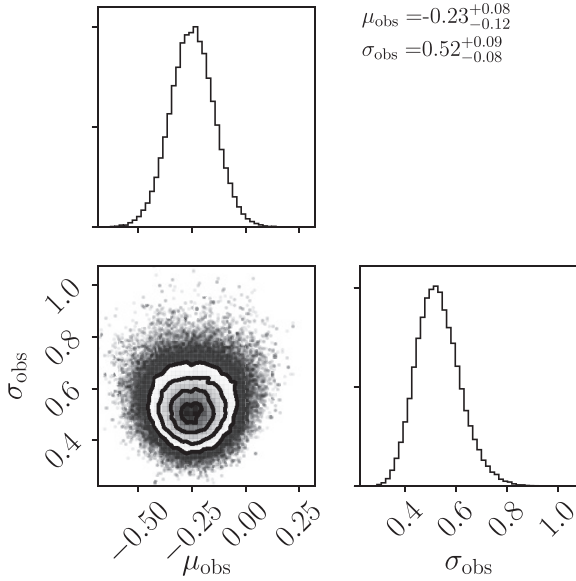


**Figure 3.** The posterior distribution for  $\mu_{\text{obs}}$  and  $\sigma_{\text{obs}}$  in  $\log_{10}(E/10^{51} \text{ erg})$ . We assume that the SN IIP explosion energies are drawn from a lognormal distribution and infer the mean and width. The mean corresponds to an energy of  $6 \times 10^{50} \text{ erg}$ , the  $1\sigma$  lower bound is  $2 \times 10^{50} \text{ erg}$ , and the  $1\sigma$  upper bound is  $2 \times 10^{51} \text{ erg}$ .

where  $P(\mu_{\text{obs}})$  and  $P(\sigma_{\text{obs}})$  are uniform priors. The likelihood for each observation is

$$\mathcal{L}(\epsilon_i | \sigma_{\epsilon,i}, \mu_{\text{obs}}, \sigma_{\text{obs}}) = \frac{1}{\sqrt{2\pi(\sigma_{\epsilon,i}^2 + \sigma_{\text{obs}}^2)}} e^{-[\epsilon_i - \mu_{\text{obs}}]^2 / [2(\sigma_{\epsilon,i}^2 + \sigma_{\text{obs}}^2)]} \quad (3)$$

To infer this posterior distribution, we use the Markov Chain Monte Carlo package EMCEE (Foreman-Mackey et al. 2013); Fig. 3 shows the posterior distribution for the model parameters; the mode and the 68 per cent highest density intervals (HDI) are  $\mu_{\text{obs}} = -0.23^{+0.08}_{-0.12}$  and  $\sigma_{\text{obs}} = 0.52^{+0.09}_{-0.08}$ . The mean corresponds to an energy of  $6 \times 10^{50} \text{ erg}$ , the  $1\sigma$  lower bound is  $2 \times 10^{50} \text{ erg}$ , and the  $1\sigma$  upper bound is  $2 \times 10^{51} \text{ erg}$ .

### 3 INFERRED EXPLOSION ENERGIES FROM CCSN SIMULATIONS

To simulate the core-collapse problem with some fidelity, CCSN simulations must include the following physics: multidimensional hydrodynamics, general relativity, dense nuclear equations of state (EOS), weak interactions, nuclear reactions, and neutrino transport. Codes that simulate all of these physics with any fidelity are computationally expensive. For example, current three-dimensional neutrino radiation hydrodynamics simulations require 10s of millions of CPU-hours; on 10 000 cores or more this requires months of computational time for just one run. As a result most codes make some approximations. Even the most advanced codes require some approximations. For the purpose of this study, we only select simulations that meet the following minimum approximations. Gravity should include at least a pseudo GR spherical potential. The neutrino transport should be a self-consistent approximation of the Boltzmann equation. Two examples of such neutrino transport are (1) solving the Boltzmann equation using discrete methods along rays and (2) solving moment equations. The transport also should

be multispecies, multigroup, and multi-angle in its approximation. The individual simulations should also show signs of approaching a final explosion energy.

The codes that satisfy these technical requirements are CHIMERA, CoCoNuT-FMT, FORNAX, PROMETHEUS-VERTEX, Zelmani, FLASH, and the Kuroda, Takiwaki & Kotake (2016) code. However, not all of these have simulations that explode and asymptotically approach a final explosion energy. Only simulations using CHIMERA, FORNAX, and CoCoNuT-FMT satisfy all conditions. The following subsections briefly describe each code and include references that include the simulation sets.

#### 3.1 Codes and simulation sets included in this study

**CHIMERA:** The full code architecture and capabilities are presented in Bruenn et al. (2006), Messer et al. (2007, 2008), and Bruenn et al. (2009, 2013, 2018). The hydrodynamics solver is a dimensionally split, Lagrangian-plus-remap Newtonian scheme with piecewise parabolic reconstruction. Self-gravity is computed by a multipole expansion and the neutrino transport is computed using ray-by-ray, with multigroup flux-limited diffusion (MGFLD) as the transport solver. The simulations of Bruenn et al. (2016) use the  $K = 220 \text{ MeV}$  incompressibility version of the Lattimer & Douglas Swesty (1991) EOS for densities  $\rho > 10^{11} \text{ g cm}^{-3}$ .

Using two-dimensional simulations, Bruenn et al. (2016) report explosions of the 12, 15, 20, and 25  $M_{\odot}$  progenitors of (Woosley & Heger 2007). Lentz et al. (2015) report the explosion of the 15  $M_{\odot}$  progenitor in three-dimensional simulations. With only one three-dimensional simulation, it is difficult to explore the trends and systematics with mass, etc. Furthermore, the simulation ends after 440 ms past bounce and 140 ms past the initiation of positive diagnostic explosion energies. The explosion energy does not start to plateau, and thus our extrapolation model for late times would be invalid in this case. Therefore, we restrict the CHIMERA sample to the two-dimensional simulations of Bruenn et al. (2016).

**CoCoNuT-FMT:** The primary description of this code's architecture is in Müller (2015). The latest advancements for this code are in Müller et al. (2019). The hydrodynamics solver for CoCoNuT-FMT solves the general relativistic hydrodynamics in spherical coordinates on a unsplit finite-volume mesh. Fluxes are calculated using an HLLC Riemann solver, and the metric equations are solved in the extended conformal flatness approximation with a spherically symmetric metric. The neutrino transport is multigroup and uses a variable Eddington factor closure and solves the transport using ray-by-ray. The transport includes gravitational redshift but neglects both velocity dependent terms and inelastic scattering. However, there is a Doppler correction to the absorption opacity.

In a three-dimensional simulation, Müller (2015) report the explosion of the 11.2  $M_{\odot}$  progenitor of Woosley, Heger & Weaver (2002); for this simulation, Müller (2015) employ the  $K = 220 \text{ MeV}$  version of the Lattimer & Douglas Swesty (1991) nuclear EOS. Using CoCoNuT-FMT and a 3D 18  $M_{\odot}$  initial progenitor to provide perturbations, Müller et al. (2017a) produced a perturbation-aided explosion. Most recently, Müller et al. (2019) produced several explosions of progenitors with zero-age main-sequence (ZAMS) masses between 9.6  $M_{\odot}$  and 12.5  $M_{\odot}$ . Since the Müller et al. (2019) study probes a sufficiently high resolution of the mass space, we choose the diagnostic energies from this set of simulations for our examination. Since there is only one model that explores perturbation-aided explosions, we do not include the results of 18  $M_{\odot}$  simulation (Müller et al. 2017a) in the final comparison



with observations. However, in Section 7, we do discuss the possible implications of perturbations on explosion energies in simulations.

**FORNAX:** The technical details and capabilities of FORNAX are presented in Skinner et al. (2018). In summary, this code solves both hydrodynamics and radiation transport using explicit, finite-volume Godunov schemes. For gravity, they use a multipole solver and replace the monopole part of the potential with a post-Newtonian approximation for GR. The transport algorithm is a multigroup, two-moment closure scheme and uses the M1 moment closure for the Eddington tensor. Both the hydro and transport components calculate the fluxes between cells using approximate Riemann solvers. Because the transport is explicit, the time-step is limited by the speed of light across the zone. In general, the speed of sound in the protoneutron star is 1/3 the speed of light, so calculating the neutrino transport explicitly only increases the number of time-steps by a factor of 3. The reductions in calculations for an explicit transport solver versus an implicit solver more than compensate for this increase in speed. In general, simulations involving FORNAX use either the  $K = 220$  MeV version of the Lattimer & Douglas Swesty (1991) EOS or the SFHo EOS (Steiner, Hempel & Fischer 2013) dense nuclear equations of state.

There are four primary publications that report CCSN explosions in FORNAX simulations. We divide them into two sets, two-dimensional simulations, FORNAX2D, and three-dimensional simulations, FORNAX3D. Radice et al. (2017) explored explodability of two-dimensional simulations for the following progenitors: n8.8, u8.1, z9.6, 9.0, 10.0, 11.0. The numbers in these models represent the zero-age main-sequence mass. All models use the  $K = 220$  MeV version of the Lattimer & Douglas Swesty (1991) EOS; they also explode in both one-dimensional and two-dimensional simulations. Vartanyan et al. (2018) simulated collapse of the 12, 13, 15, 16, 17, 19, 20, 21, and 25  $M_{\odot}$  progenitors (Woosley & Heger 2007). For these simulations, they use the SFHo EOS (Steiner et al. 2013). They reported explosions for the 16, 17, 19, and 20  $M_{\odot}$  progenitors, but only the 16, 17, and 19  $M_{\odot}$  progenitors provide diagnostic explosion energies that are greater than zero and approach an asymptotic value. Vartanyan et al. (2019) simulated three-dimensional collapse and explosion of the 16  $M_{\odot}$  progenitor. They find an explosion, but this simulation has yet to reach positive diagnostic explosion energies. More recently, Burrows et al. (2019) simulate the three-dimensional explosions for the same 9, 10, 11, 12, and 13  $M_{\odot}$  progenitors but using the SFHo EOS (Steiner et al. 2013). For the progenitors that are simulated both in two and three dimensions, the explosion time and diagnostic explosion energies are very similar.

### 3.2 Codes and simulations not included in this study

**PROMETHEUS-VERTEX:** Melson et al. (2015a) describe the code architecture for this code. The hydrodynamics algorithm is a finite-volume Godunov scheme using Riemann solvers to calculate fluxes. For gravity, the code solves the multipole expansion and replaces the monopole with a pseudo potential that represents a post-Newtonian approximation to GR. The neutrino transport solves the Boltzmann equation on radial rays.

There are two three-dimensional explosions using Prometheus-Vertex. Melson et al. (2015a) report the three-dimensional explosion of a 9.6  $M_{\odot}$  star. In the same year, Melson et al. (2015b) report the three-dimensional explosion of a 20  $M_{\odot}$  star. These represent the first self-consistent three-dimensional explosions. However, the latter is not what one would consider a fiducial simulation; it

explores strange-quark contributions to the neutrino–nucleon scattering. The former does explode and begins to approach asymptotic values at about 400 ms past bounce or 300 ms past the initiation of explosion. The final reported explosion energy is  $0.1 \times 10^{51}$  erg, and the final rate of increase is about  $10^{51}$  erg  $s^{-1}$ . Summa et al. (2016) simulated the explosion of 18 progenitors in two-dimensional simulations. However, they only reported diagnostic explosion energies for four of the progenitors, and these did not reach asymptotic values in the explosion energy. With only one simulation reaching the final phase of the explosion, it is difficult to make any systematic conclusions about the performance of Prometheus-Vertex simulations. Therefore, we do not include Prometheus-Vertex results at this time.

**FLASH:** O’Connor & Couch (2018) include approximate GR in FLASH, a finite-volume hydrodynamics code. The gravity algorithm solves the Newtonian Poisson’s equation via a multipole solver and replaces the monopole term with a post-Newtonian pseudo-GR potential. The neutrino transport solves the two-moment equations and uses the M1 closure. The transport is also multigroup, includes velocity dependence and inelastic scattering.

Using FLASH, O’Connor & Couch (2018) simulated the collapse of the 12, 15, 20, and 25  $M_{\odot}$  progenitors (Woosley & Heger 2007). The 15, 20, and 25  $M_{\odot}$  runs exploded, reaching explosion energies ranging from 0.15 to  $0.25 \times 10^{51}$  erg. However, none reach the plateau phase in diagnostic explosion energy, so we are not able to include these results in our comparison.

**Zelmani:** Roberts et al. (2016) present the code architecture. Zelmani is a three-dimensional GR, multigroup radiation-hydrodynamics code. The neutrino transport solves the two-moment equations and uses an M1 closure. Zelmani also neglects velocity dependence and inelastic scattering processes. Ott et al. (2018) simulated the explosions of 12, 15, 20, 27, and 40  $M_{\odot}$  progenitor models of Woosley & Heger (2007) and with the SFHo (Steiner et al. 2013) EOS. Though the fidelity of this code meets the requirements of our analysis, the simulations terminated very shortly after explosion, and so the explosion curves are far from their plateau phase. Thus, we are not able to include these simulations in this study.

**Kuroda (2016):** The code presented in Kuroda et al. (2016) meets some of the technical requirements. The neutrino transport is multigroup and is a two-moment scheme using the M1 closure. The code solves the GR field equations. They simulated collapse of a 15  $M_{\odot}$  progenitor. However, this simulation did not explode.

**Codes Using IDSA:** Some investigations use an approximation to neutrino transport called isotropic diffusion source approximation (IDSA) (Liebendörfer, Whitehouse & Fischer 2009). IDSA was designed as a fast approximation to multidimensional neutrino transport. In general, it transports energy and lepton number, and while its speed enables innovative and systematic investigations, the approximations within this scheme must be calibrated against Boltzmann-transport based schemes. Since the IDSA is calibrated against Boltzmann transport but is not a scheme directly derived from Boltzmann transport, we do not include IDSA simulations in our comparison. If future comparisons thoroughly validate the IDSA scheme, then IDSA simulations would prove valuable tools in rapidly and systematically exploring explosions. For example, Nakamura et al. (2015) performed a large (101 simulations) systematic investigation of two-dimensional CCSN simulations. In general, they found that most progenitors explode. Although, they did not report the diagnostic explosion energies for most of these simulations.

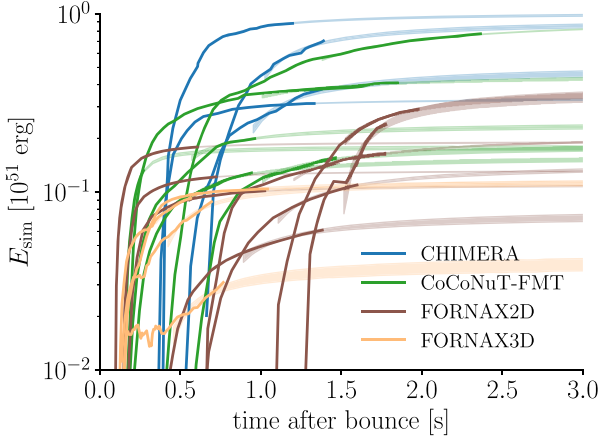


**Figure 4.** Simulated explosion energies ( $E_{\text{sim}}$ ) versus time after bounce. The thick solid lines represent the diagnostic explosion energies for CHIMERA (blue), CoCoNuT-FMT (green), FORNAX2D (brown), and FORNAX3D (yellow). Assuming that the growth of explosion energy is dominated by neutrino power, we propose a simple extrapolation of the explosion energy curve. See equation (5). The wide bands represent a 68 percent confidence interval extrapolation. From this extrapolation we infer an explosion energy after infinite time,  $E_{\infty}$ . The model appears to be a good fit for nearly all simulations except the very underenergetic model in the FORNAX3D set. That simulation corresponds to the  $10.0 M_{\odot}$  progenitor and is likely still developing the explosion profile even after 750 ms.

#### 4 EXTRAPOLATING SIMULATED EXPLOSION ENERGIES TO LATE TIMES

The explosion energies in many of the multidimensional simulations are still increasing when the simulations terminate. At the same time, most appear to be approaching an asymptotic value. Therefore, at best, the reported diagnostic explosion energies are a minimum. Here, we note that the energy evolution for all simulations follows a common functional form. We suggest a simple model for explosions driven by neutrino heating. This model leads to a simple functional form that is a good fit to the simulations. Here, we use this functional form to extrapolate the explosion energy to infinite time,  $E_{\infty}$ .

Fig. 4 shows the diagnostic explosion energies in units of  $10^{51}$  erg as a function of time after bounce. The solid lines represent the results of multidimensional simulations, and the bands at the end of each curve represents our extrapolation. Blue represents CHIMERA simulations, green represents CoCoNuT-FMT, brown represents FORNAX2D, and yellow represents FORNAX3D. All curves rise and show signs of asymptotically approaching a finite explosion energy,  $E_{\infty}$ . In a preliminary analysis, we considered two functional forms: an exponential and a power law. These crude initial comparisons suggest that the energy curves asymptote via a power law and not an exponential. Using this crude analysis as a guide, we now suggest a model for the explosion energy curve and derive the functional form.

If neutrinos are primarily driving the explosion, then one might expect the rate of growth of explosion energy to be roughly proportional to the neutrino power.

$$\frac{dE_{\text{exp}}}{dt} \approx L_{\nu} \tau, \quad (4)$$

where  $L_{\nu}$  is the neutrino luminosity and  $\tau = \int \rho \kappa dr$  is the optical depth to neutrino absorption in the region of net neutrino

heating.  $\kappa$  is the neutrino absorption cross-section per unit mass,  $\kappa \approx \sigma/m_p$ .

A few straightforward assumptions lead to a simple function for  $E_{\text{sim}}(t)$ . First, during the explosion, we assume that the optical depth is roughly  $\tau \sim \kappa M_{\text{gain}}/R_s^2$ , where  $M_{\text{gain}}$  is the mass in the gain region and  $R_s$  is the shock radius. Making the simplest assumptions, we assume that  $L_{\nu}$  and  $M_{\text{gain}}$  are roughly constant during the last stage of explosion development. In addition, we assume that  $R_s = v_s t$ , and that the shock velocity,  $v_s$  is also constant. Integrating equation (4) leads to the following functional form

$$E_{\text{exp}}(t) = E_{\infty} - \frac{A}{t}, \quad (5)$$

Formally,  $A$  is proportional to  $L_{\nu} \kappa M_{\text{gain}}/v_s^2$ , but we do not have access to these values for all of the simulations. Therefore, in our extrapolations, we fit only for two parameters,  $E_{\infty}$  and  $A$ .

We use Bayesian inference to find the best-fitting values for  $E_{\infty}$  and  $A$ . The posterior distribution for  $E_{\infty}$  and  $A$  is

$$P(E_{\infty}, A, \sigma | \{E_{\text{sim},i}\}) \propto \mathcal{L}(E_{\text{sim},i} | E_{\infty}, A, \sigma) P(E_{\infty}) P(A) P(\sigma). \quad (6)$$

It is unclear what the variance  $\sigma^2$  is for the simulations. Therefore, we include  $\sigma$  as an unknown nuisance parameter and simply marginalize over all possible values to infer the posterior distribution for  $E_{\infty}$  and  $A$ ,  $P(E_{\infty}, A)$ . With little prior information about any of these parameters, we choose uniform priors for  $P(E_{\infty})$ ,  $P(A)$ , and  $P(\sigma)$ . To model the likelihood, we assume a Gaussian distribution for each simulation data point:

$$\mathcal{L}(\{E_{\text{sim},i}\} | E_{\infty}, A) = \prod_i \mathcal{N}_i(E_{\text{sim},i} | E_{\text{exp}}(t_i, E_{\infty}, A), \sigma), \quad (7)$$

where

$$\begin{aligned} \mathcal{N}_i(E_{\text{sim},i} | E_{\text{exp}}(t_i, E_{\infty}, A), \sigma) \\ = \frac{1}{\sqrt{2\pi}\sigma} e^{-[E_{\text{sim},i} - E_{\text{exp}}(t_i, E_{\infty}, A)]^2 / [2\sigma^2]}. \end{aligned} \quad (8)$$

The mean is the modelled explosion energy,  $E_{\text{exp}}(t)$  equation (5). The unknowns to infer are the asymptotic explosion energy,  $E_{\infty}$ , the parameter for the  $1/t$  term,  $A$ , and the unknown variation within each simulation,  $\sigma$ .

When inferring these parameters, we only fit the last half of the energy curve. The primary assumptions of the evolution model assume that  $L_{\nu}$ ,  $M_{\text{gain}}$ , and  $v_s$  are constant. If these assumptions are appropriate at all, they are likely valid in the last part of the explosion energy evolution. To perform these inferences, we use Markov Chain Monte Carlo Bayesian inference package emcee (Foreman-Mackey et al. 2013). The bands extrapolating the energy curves in Fig. 4 show the resulting inferences. The width of the band represents the 68 percent highest density confidence interval (HDI) for these fits.

Table 2 summarizes the set of simulation explosion energies. The first row gives the progenitor as presented in the simulation papers. Each progenitor name conveniently indicates the ZAMS mass in  $M_{\odot}$ . The second column reports the final explosion energy of the simulation,  $E_{\text{sim}}(t_{\text{end}})$ . The third column presents the end of the simulation in seconds after bounce,  $t_{\text{end}}$ . Finally, column four shows the mode of the extrapolated explosion energy,  $E_{\infty}$ .

The four panels in Fig. 5 compare  $E_{\infty}$  with an estimate for the observed explosion energies. The vertical lines indicate the estimated simulation explosion energy. The height of the lines are proportional to  $M^{-2.35}$ , representing the initial mass distribution. In

**Table 2.** Explosion energies for two-dimensional and three-dimensional CCSN simulations. The simulations for CHIMERA are two-dimensional, CoCoNuT-FMT are three-dimensional, FORNAX2D are two-dimensional, and FORNAX3D are three-dimensional. The 18ProgConv model represents the explosion of the  $18 M_{\odot}$  progenitor that includes pre-collapse perturbations due to O-shell burning (Müller et al. 2017a). Since the initial conditions are different from the other CoCoNuT-FMT simulations, we do not include 18ProgConv in the rest of the explosion energy analysis. However, we do discuss the possible ramifications of progenitor convection in Section 7. See the text for references and further discussion.

Progenitor	$E_{\text{sim}}(t_{\text{end}})$ ( $10^{51}$ erg)	$t_{\text{end}}$ (s)	$E_{\infty}$ ( $10^{51}$ erg)
CHIMERA			
12	0.31	0.97	0.34
15	0.88	0.81	1.03
20	0.38	0.84	0.50
25	0.70	0.73	0.93
CoCoNuT-FMT			
11.2	0.13	0.77	0.16
s11.8	0.20	0.78	0.24
s12.5	0.16	0.90	0.19
z12	0.41	1.68	0.47
z9.6	0.13	0.12	0.18
18ProgConv	0.77	1.96	0.98
FORNAX2D			
11.0	0.11	0.98	0.15
9.0	0.06	0.98	0.08
n8.8	0.18	0.51	0.19
u8.1	0.10	0.85	0.11
z9.6	0.12	0.58	0.13
16	0.16	1.13	0.21
17	0.29	0.90	0.39
19	0.24	0.52	0.39
FORNAX3D			
9.0	0.10	0.91	0.11
10.0	0.03	0.62	0.04
11.0	0.09	0.44	0.12
12.0	0.09	0.54	0.12

other words, the height represents the fraction of stars that would explode with that energy within the simulated set. The gray lines in each represent the ‘marginalized’ inferred explosion energies from observations (Pejcha & Prieto 2015). The term marginalized is in quotes because without the original posterior distributions, we performed a crude marginalization using fig. 2 from Pejcha & Prieto (2015). The fraction  $f_{25}$  in each figure represents the fraction of the IMF that each code has simulated from  $7.4$  to  $25 M_{\odot}$ . The minimum corresponds to the minimum mass for CCSNe (Díaz-Rodríguez et al. 2018), the maximum corresponds to the maximum mass for SN IIP (Smartt 2015; Davies & Beasor 2018). For further discussion on these limits see Section 7.

Upon first glance, the CHIMERA set appears to be most consistent with the observations, and the FORNAX sets are the least consistent. However, the CHIMERA simulations mostly use the highest mass progenitors. Below, we note a correlation between explosion energy and progenitor mass for the FORNAX2D set. Therefore, the CHIMERA results may actually represent the highest explosion energies when a full range of progenitors are considered. In other words, the range of progenitor masses simulated represents a possible bias for each simulation set. Below, we model the explosion energy as a function of progenitor mass to account for this possible bias.

## 5 INFERRING THE FULL SIMULATION EXPLOSION ENERGY DISTRIBUTION

The simulation sets have not yet sampled the whole range of progenitors from  $7.4$  to  $25 M_{\odot}$ . Therefore, the explosion energies in Table 2 represent a biased sample. For example, Fig. 6 plots  $E_{\infty}$  (dots) versus progenitor mass. It is apparent that the CHIMERA set includes mostly high-mass progenitors, the CoCoNuT-FMT set includes mostly the middle, and the FORNAX2D set has simulated a larger range. Note that the 18ProgConv model (green square) is omitted in the analysis for CoCoNuT-FMT. In this section, we infer a relationship between explosion energy and progenitor mass. Then, we use this inference to infer the full distribution of explosion energies between  $7.4$  and  $25 M_{\odot}$ .

The simplest assumption is that the explosion energy is proportional to some power of the progenitor mass. In fact, Poznanski (2013) suggest that  $E_{\text{exp}} \propto M^2$ . They noted that all plateau durations are about the same. In addition, the observed luminosities and velocities are correlated with a scaling of  $L \propto v^2$  (Hamuy & Pinto 2002). These two observations led Poznanski (2013) to suggest a correlation between explosion energy and progenitor mass. Using scaling relations, Poznanski (2013) suggest a correlation of  $E_{\text{exp}} \propto M^3$ . Interpolating in light-curve models, they found a slightly different correlation of  $E_{\text{exp}} \propto M^2$ . Using a different approach Chugai & Utrobin (2014) found a similar conclusion. They modelled the oxygen production of 11 SNe IIP and suggested a correlation but did not give the specific scaling. More recently, Pejcha & Prieto (2015) quantified this correlation using 19 SN IIP light-curve models; they infer that the explosion energy is proportional to a power of the ejecta mass,  $E_{\text{exp}} \propto M_{\text{ej}}^{1.81^{+0.45}_{-0.34}}$ .

Therefore, the most natural model to assume for the correlation is

$$\log(E_{\infty}/10^{51} \text{ erg}) = \beta_0 + \beta_1 \log(M/10 M_{\odot}). \quad (9)$$

To infer the parameters,  $\beta_0$  and  $\beta_1$ , we use EMCEE (Foreman-Mackey et al. 2013) to infer the following posterior distribution

$$P(\beta_0, \beta_1, \sigma | \{E_{\infty, i}\}, \{M_i\}) \propto \prod_i \mathcal{L}(E_{\infty, i} | M_i, \beta_0, \beta_1, \sigma) P(\beta_0) P(\beta_1) P(\sigma), \quad (10)$$

where the likelihood for the simulated explosion energy  $E_{\infty, i}$  is

$$\mathcal{L}(E_{\infty, i} | M_i, \beta_0, \beta_1, \sigma) = \frac{1}{\sqrt{2\pi}\sigma} e^{-[\log(E_{\infty, i}/B) - \beta_0 - \beta_1 \log(M_i/M_{\odot})]^2 / (2\sigma^2)}. \quad (11)$$

The variation in the simulated energies,  $\sigma$ , is an unknown nuisance parameter. The priors,  $P(\beta_0)$ ,  $P(\beta_1)$ , and  $P(\sigma)$ , are all assumed to be uniform.

Fig. 7 shows the posterior distribution for the FORNAX2D simulation set. The marginalized parameters are  $\beta_0 = -0.85 \pm 0.06$  and  $\beta_1 = 1.52^{+0.36}_{-0.48}$ . The values are the modes, and the uncertainties are the 68 per cent highest density intervals (HDI). For the CHIMERA, CoCoNuT-FMT, and FORNAX3D simulation sets, there are far too few simulations to adequately constrain the slope. Therefore, we use the  $\beta_1$  distribution for FORNAX2D as the prior for the other two sets. The marginalized parameters for CHIMERA are  $\beta_0 = -0.52^{+0.19}_{-0.22}$  and  $\beta_1 = 1.45^{+0.40}_{-0.38}$ ; the marginalized parameters for CoCoNuT-FMT are  $\beta_0 = -0.73 \pm 0.11$  and  $\beta_1 = 1.49^{+0.46}_{-0.35}$ ; the marginalized parameters for FORNAX3D are  $\beta_0 = -1.07 \pm 0.17$  and  $\beta_1 = 1.56^{+0.36}_{-0.46}$ . The inference for CoCoNuT-FMT does not include the 18ProgConv model. The lines in Fig. 6 represent the

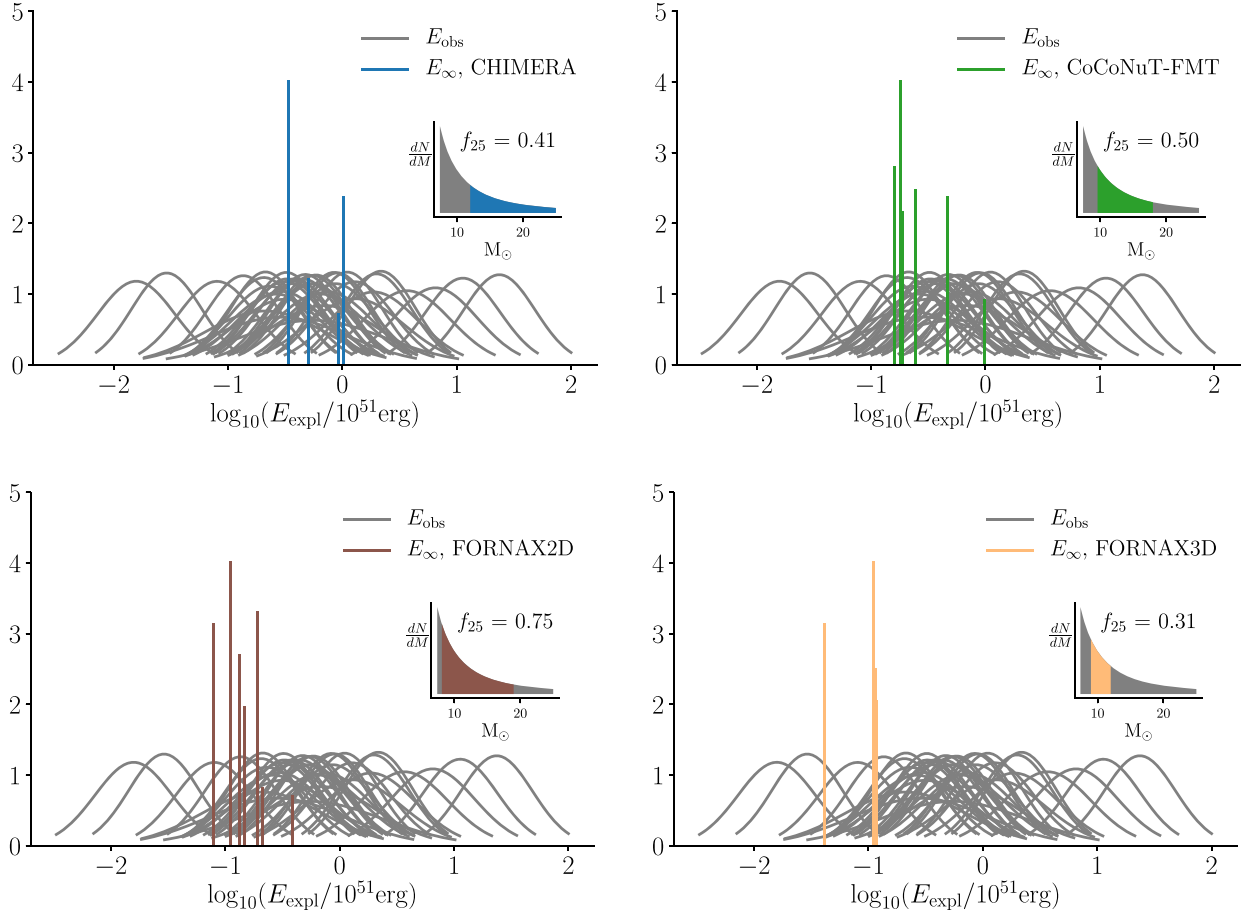


**Figure 5.** The probability density functions for  $E_{\text{obs}}$  and  $E_{\infty}$ .  $E_{\text{obs}}$  is an estimate for the marginalized observed explosion energy from Pejcha & Prieto (2015).  $E_{\infty}$  represents the extrapolated explosion energies for four simulation sets: CHIMERA represents the two-dimensional simulations of Bruenn et al. (2016); CoCoNuT-FMT represents the three-dimensional simulations of Müller (2015), Müller et al. (2017a), and Müller et al. (2019); FORNAX2D represents the two-dimensional simulations of Radice et al. (2017) and Vartanyan et al. (2018); FORNAX3D represents the three-dimensional simulations of Burrows et al. (2019). The heights of  $E_{\infty}$  represent a weighting due to the IMF. The inset and  $f_{25}$  represents the fraction of the IMF that the simulations have sampled between 7.4 and 25  $M_{\odot}$ . This range roughly represents the expected progenitors for SN IIP.

distribution of possible functions. For each MCMC sample of  $\beta_0$  and  $\beta_1$ , we calculate  $E_{\infty}$  as a function of  $M$ . Then, we calculate the 68 percent HDI for  $E_{\infty}$ . Within the confidence intervals, the exponent ranges from linear to quadratic,  $E_{\infty} \propto M^{1-2}$ .

Using observations, Pejcha & Prieto (2015) infer the relationship between the explosion energy ( $E_{\text{exp}}$  in their manuscript) and the ejecta mass  $M_{\text{ej}}$ . Since the neutron star that is left behind is only 1.4  $M_{\odot}$ , and there is not much mass loss for the red supergiant progenitors they consider, the ejecta mass is similar to the ZAMS progenitor mass. They find that  $E_{\text{exp}} \propto M_{\text{ej}}^{1.81^{+0.45}_{-0.34}}$ , which is consistent with our inference.

Next, we extrapolate to infer the explosion energy distribution for the range of progenitor masses between 7.4 and 25  $M_{\odot}$ . The posterior for the explosion energies is

$$P(E_{\infty}) = \int P(E_{\infty}|\beta_0, \beta_1, \sigma, M) \cdot P(\beta_0, \beta_1, \sigma) \cdot P(M) dM d\beta_0 d\beta_1, \quad (12)$$

where  $P(\beta_0, \beta_1, \sigma)$  is the posterior distribution, equation (10), for the model parameters, and  $P(M)$  is the progenitor mass distribution. For this study, we assume that  $P(M) \propto M^{-2.35}$ . To determine  $P(E_{\infty})$ , we take a sample of  $(\beta_0, \beta_1, \sigma)$  from MCMC posterior distribution,

draw a mass from the IMF distribution,  $P(M) \propto M^{-2.35}$ , and evaluate  $E_{\infty}$  using equation (9). The resulting distributions for each code are in Fig. 8. On average, all simulations sets exhibit explosion energies that are significantly lower than the observations. In the next section, we quantify the difference between simulations and observations.

## 6 COMPARING OBSERVATIONS WITH MULTIDIMENSIONAL SIMULATIONS

Since the average explosion energies of the simulations are lower than the observations, we develop a model to infer the missing explosion energy,  $\Delta = \log(E_{\text{obs}}/E_{\infty})$ . For compactness and readability in the following equations, we define  $\epsilon = \log(E/10^{51} \text{ erg})$ . The posterior distribution for  $\Delta$  is

$$P(\Delta|\{\epsilon_{\text{obs},i}\}) \propto \prod_i \int P(\epsilon_{\text{obs},i}|\epsilon_{\infty}, \Delta) P(\epsilon_{\infty}|M) P(M) P(\Delta) d\epsilon_{\infty} dM. \quad (13)$$

We assume a uniform prior for  $\Delta$ ,  $P(\Delta)$ . This posterior distribution represents a hierarchical Bayesian inference where  $\epsilon_{\infty}$  and  $M$  are intermediate nuisance parameters. The portion of the likelihood that is  $P(\epsilon_{\infty}) = \int P(\epsilon_{\infty}|M) P(M) dM$  has already been calculated and



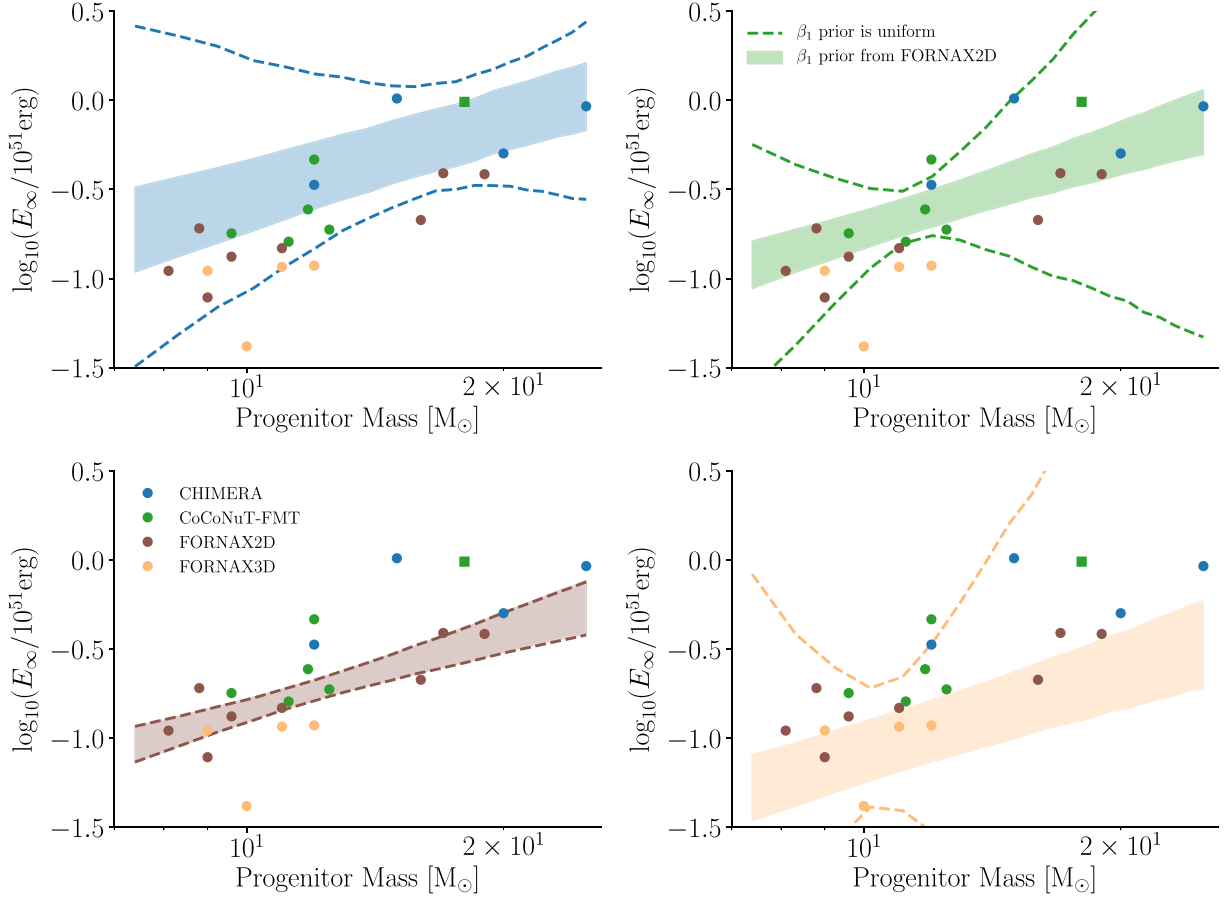


**Figure 6.** Extrapolated explosion energy for simulations versus progenitor mass. CCSN simulations are computationally expensive, and so there are few simulations to compare to observations. SN IIP are expected to have progenitor masses between 7.4 and 25  $M_{\odot}$ . Therefore, we infer a function relating  $E_{\infty}$  to the progenitor mass. Later, we use this function to infer the distribution of simulated explosion energies between 7.4 and 25  $M_{\odot}$ . We fit a line in log space. The region between the dashed lines represent the 68 per cent confidence interval for this slope. For all sets except FORNAX2D, there are too few simulations to constrain the slope. The solid band represents the 68 per cent confidence interval when using the slope from the FORNAX2D set as a prior for the other sets. The green square represents the 18ProgConv model of the CoCoNuT-FMT set, and since it is the only model that includes perturbations due to O-shell burning, it is not included in the explosion energy versus mass fit.

is shown in Fig. 8. Since the distributions for  $P(\epsilon_{\infty})$  are essentially Gaussian, we use the Gaussian approximation for  $P(\epsilon_{\infty})$ . With this approximation, the marginalization over the nuisance parameters in equation (13) is analytic, and the likelihood is now given by

$$\mathcal{L}(\epsilon_{\text{obs},i} | \epsilon_{\infty}, \Delta) = \frac{1}{\sqrt{2\pi(\sigma_{\text{obs}}^2 + \sigma_{\infty}^2)}} e^{-[\epsilon_{\text{obs},i} - \mu_{\infty} - \Delta]^2 / [2(\sigma_{\text{obs},i}^2 + \sigma_{\infty}^2)]}, \quad (14)$$

where  $\mu_{\infty}$  is the mode of  $P(\epsilon_{\infty})$ , and  $\sigma_{\infty}$  is the half width of the 68 per cent HDI.

Fig. 9 shows the inferred  $\Delta$  distributions for the four simulation sets. For CHIMERA,  $\Delta = 0.25 \pm 0.07$ ; for CoCoNuT-FMT,  $\Delta = 0.49 \pm 0.07$ ; for FORNAX2D  $\Delta = 0.62 \pm 0.06$ ; for FORNAX3D  $\Delta = 0.85 \pm 0.07$ . All three simulation sets have more than 99.9 per cent of their distributions,  $P(\Delta)$ , greater than zero. Based upon the models and assumptions in this manuscript, all three simulation sets have explosion energies that are significantly smaller than observations. In the best case (CHIMERA), the simulated explosion energies are a factor 2 less energetic than the observed energies. In the worst case (FORNAX3D), the simulated explosion energies are a factor of 10 less energetic.

## 7 DISCUSSION AND CONCLUSIONS

In general, we find that the explosion energies of multidimensional simulations are significantly less energetic than the explosion energies inferred from observations. For this comparison, we require the CCSN simulations and codes to have the following attributes; two- or three-dimensional, neutrino transport that is a self-consistent approximation of Boltzmann transport equations, transport is multi-angle and multispecies, general relativity or some post-Newtonian approximation, and positive explosion energies, approaching asymptotic values. The codes that satisfy these requirements are CHIMERA, CoCoNuT-FMT, and FORNAX. For the inferred observational explosion energies, we use the light-curve parameters of 40 SN IIP (Pejcha & Prieto 2015; Müller et al. 2017b) and the fitting formula of Goldberg et al. (2019). Inferring the observed explosion parameters requires constraints on the radius of the progenitor, which is rarely available for observed SNe. To resolve this, we use the radii of 581 RSGs as a prior (Davies et al. 2018) and infer the explosion energies of the 40 SN IIP. We infer a mean observational explosion energy of  $\mu_{\text{obs}} = -0.23^{+0.08}_{-0.12}$  in units of  $\log_{10}(E_{\text{obs}}/10^{51} \text{ erg})$ ; the width of the distribution is  $\sigma_{\text{obs}} = 0.52^{+0.09}_{-0.08}$ . To compare the observations and simulations, we infer the ratio of observed-to-simulated explosion energies,

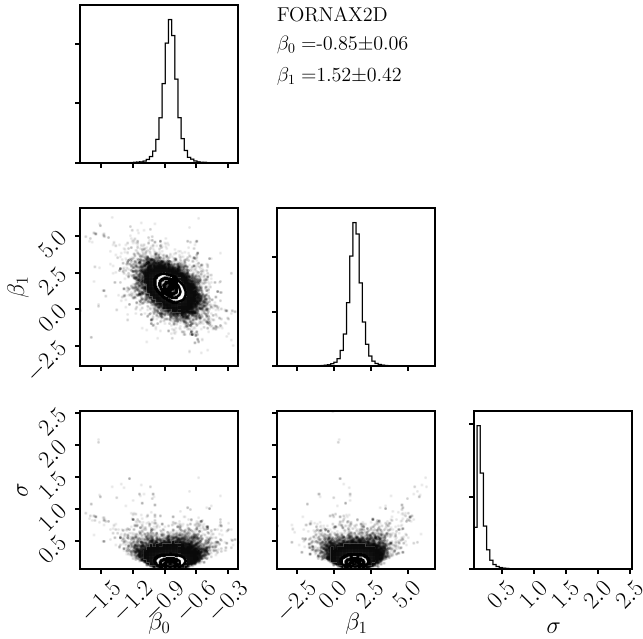


**Figure 7.** Posterior distribution for the fitting parameters in explosion energy as a function of progenitor mass.  $\beta_0$  is the explosion energy of a  $10 M_\odot$  progenitor, and  $\beta_1$  is the power-law slope. See equation (9) for the definition of these parameters. This posterior distribution is for the FORNAX2D simulation set.

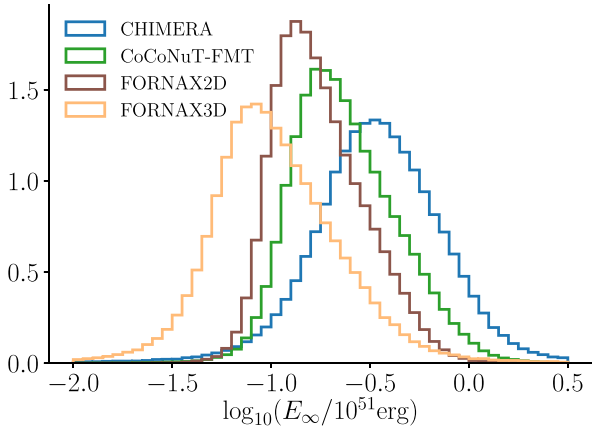


**Figure 8.** Posterior distribution of simulated explosion energies for each simulation set. This inference assumes that every progenitor between  $7.4$  and  $25 M_\odot$  explodes and that the explosion energy is a function of progenitor mass as given by equation (9) and the fits in Figs 6 and 7.

$\Delta = \log_{10}(E_{\text{obs}}/E_\infty)$ , where  $E_\infty$  is our estimate of the simulation energy extrapolated to infinite time. For CHIMERA,  $\Delta = 0.25 \pm 0.07$ , for CoCoNuT-FMT,  $\Delta = 0.49 \pm 0.07$ , for FORNAX2D,  $\Delta = 0.62 \pm 0.06$ , and for FORNAX3D,  $\Delta = 0.85 \pm 0.07$ . Overall, all simulation sets are less energetic than the explosion energies inferred from observations.

This result suggests a tension between the simulations and observations. However, it does not yet rule out the standard neutrino mechanism. Of the four simulation sets, the mean offset is  $\Delta \approx 0.6$ , but the range goes from 0.25 to 0.85, and the width of this range is 0.6. In other words, the variance is of order the average offset. Given this, it is plausible that future improvements to the simulations might resolve the current discrepancy. Of all

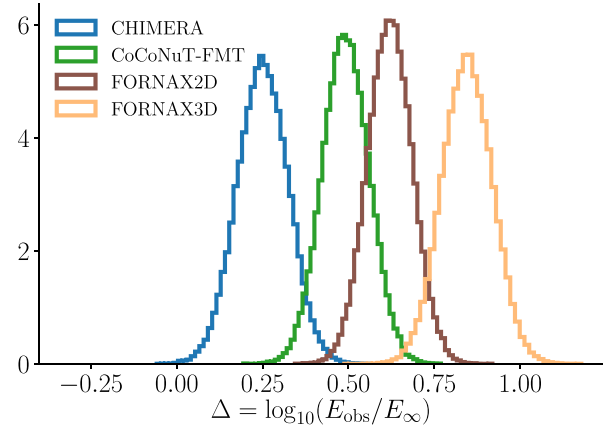


**Figure 9.** Posterior distributions comparing observational and simulated explosion energies. All three codes produce simulation energies that are significantly lower than explosion energies inferred from observations. For CHIMERA,  $\Delta = 0.25 \pm 0.07$ , for CoCoNuT-FMT  $\Delta = 0.49 \pm 0.07$ , for FORNAX2D,  $\Delta = 0.62 \pm 0.06$ , and for FORNAX3D,  $\Delta = 0.85 \pm 0.07$ . The mean  $\Delta$  for all simulations is 0.6; the variation for the simulations ranges from 0.25 to 0.85 (width of 0.6). The variation among the simulations is as large as the mean offset. While there is a tension between the simulations and observations, the large variation among simulations suggests that further improvements to simulations could resolve this discrepancy.

the possible explosion mechanisms, the neutrino mechanism is the only first-principles theory that produces predictions that can be compared to observations. From this perspective, a factor of 4 tension could be viewed as a good first step in making quantitative comparisons between theory and observations.

In this analysis, we identify several biases in the simulation sets. Core-collapse simulations are computationally expensive, and few of the results include large systematic studies of the full range of progenitors. Furthermore, most simulations terminate well before an asymptotic explosion energy.

To mitigate for these biases in the simulation sets, we model the distribution of explosion energies from simulations. The FORNAX2D results exhibit the largest sample, so we use their results to infer an explosion energy versus progenitor mass relationship. Our inference shows that  $E_\infty \propto M^{1-2}$ ; the simulation explosion energies are proportional to progenitor mass with a power ranging from linear to quadratic. To infer the simulation explosion energy after infinite time, we fit a simple model,  $E_{\text{sim}}(t) = E_\infty - A/t$ , that is motivated by a simple neutrino-powered explosion. Then, we assume that all models between the  $7.4 M_\odot$  and  $25 M_\odot$  explode. This range includes the minimum mass for CCSN explosions (Díaz-Rodríguez et al. 2018) and a rough estimate for the maximum progenitor for SN IIP (Smartt 2015; Davies & Beasor 2018).

Better estimates for the simulated explosion energy distribution will require more systematic explorations between  $7.4$  and  $25 M_\odot$ , and better estimates will require simulations that terminate later. Based upon our simple model, simulations must evolve roughly  $0.5$ – $2$  s past the time of positive explosion energies to reach at least 90 per cent of the asymptotic explosion energy.

There are other potential biases in the simulations which are either difficult to quantify in this study or have yet to be identified at all. For example, resolution of the grid may impact whether CCSN simulations have converged. Recently, Melson & Janka (2019) explore how resolution affects turbulence in simplified three-dimensional CCSN simulations, but these explorations do not address how resolution affects the explosion energies. A major difference among

the codes is the treatment of neutrino transport. There are many approximations and choices in the transport: ray-by-ray versus multi-angle, energy groups, moments versus short characteristics, moment closures, velocity-dependent terms, gravitational redshift, scattering opacities, correlated opacities, etc. In fact, there are more different choices in the neutrino transport treatment than there are codes. Yet, it is unclear how these differences impact the explosion energies.

Progenitor perturbations due to O-shell burning may be important in reducing the tension between simulations and observations. The majority of simulations that are available do not include progenitor perturbations, but the one model that does, offers some tantalizing clues. The 18ProgConv model of the CoCoNuT-FMT set has the largest explosion energy of that set. If we include this one model, then the discrepancy reported for CoCoNuT-FMT does not actually change much. The lack of change is because this model has a relatively high mass. The explosion energy versus progenitor mass correlation already indicates that the higher masses explode with higher energy. Including 18ProgConv in the fit only steepens the dependence a little. In addition, the highest masses are more rare and provide little weighting to the final explosion energy distribution. So, this one perturbation-aided explosion does not change  $\Delta$  for CoCoNuT-FMT.

However, it is not clear what progenitor perturbations would do for the lower mass progenitors. Müller et al. (2017a) report a difference in explosion time depending upon the size of the progenitor perturbations. They simulated three  $18 M_{\odot}$  progenitors models: one with no O-shell perturbations, one with a convective mach number of 0.04, and one with a convective mach number of 0.1. The first did not explode by 650 ms after bounce, the second exploded at around 500 ms, and the largest perturbations exploded at 300 ms. They only show the inferred explosion energy for the largest perturbations, so we do not have a quantitative measure of how perturbations affect the explosion energy. None the less, an earlier explosion might lead to higher explosion energies. To test whether progenitor perturbations affect the explosion energies, we recommend that simulators perform a systematic study of progenitor perturbations for a wide range of masses.

Throughout this manuscript, we are careful to note that the explosion energies that represent the observations are not observations in themselves, but are inferences based upon observations. As such, the ‘observed’ explosion energies are also subject to biases.

A significant source of systematic uncertainty in modelling the photospheric properties is the zero point in the fitting formulae. Goldberg et al. (2019) summarize the zero points for several studies (Popov 1993; Kasen & Woosley 2009; Sukhbold et al. 2016; Goldberg et al. 2019); see the discussion just after equation (7) in their manuscript. They find that the systematic uncertainty in the luminosity zero points is about 0.09 in log base 10. This translates to a systematic uncertainty in the log of the explosion energy of 0.1. While this is not enough to completely account for the discrepancy between the simulations and observations, it is of the same order. In addition, Dessart & Hillier (2019) and Goldberg et al. (2019) caution that there are significant degeneracies among the explosion parameters: nickel mass, ejecta mass, explosion energy, and progenitor radius. In fact, Goldberg et al. (2019) argue that one other observational parameter besides  $M_V$ , velocity, and  $t_p$  is required to break this significant degeneracy. In this manuscript, we use the radii of RSGs as a prior, and while this provides some constraints, having the progenitor’s radius would further constrain the observed explosion energy.

Dessart & Hillier (2019) highlight another source of degeneracy when inferring the initial progenitor mass from light curves. The light curve of SN IIP depend mostly on the H-envelope mass and is insensitive to the He-core mass. While the He-core mass depends upon the initial progenitor mass, the H-envelope mass is mostly sensitive to mass-loss prescriptions. Since the mass-loss prescriptions are uncertain, this degeneracy presents a systematic uncertainty when inferring the progenitor mass from light curves.

Another potential source of bias for the observational set is the sample of SNe. At the moment, most modellers infer explosion energies by modelling light curves of type IIP SNe. For this analysis, we assume that all progenitors between  $7.4$  and  $25 M_{\odot}$  explode as type IIP SNe. However, it is not clear what fraction of this mass range corresponds to IIL or even Ib/Ic. The recent progenitor mass inferences of 25 historic SNe (Williams et al. 2018) suggest that at least some fraction of this range do correspond to these other SN types. SN surveys suggest that SN IIP are only  $48.2^{+5.7}_{-5.6}$  per cent of all CCSNe (Smith et al. 2011). At the moment, it is not clear if this fraction is a result of a mass dependence or binary evolution. Whatever the case may be, there is a clear bias in the observed explosion energies for a sub sample of CCSNe. One strategy to mitigate against this potential source of bias would be to model the explosion energies of all SN types within a volume-limited sample. To do this, light-curve models must include the other SN types, not just SN IIP.

In summary, we find that the explosion energies of multidimensional CCSN simulations are significantly lower than the energies inferred from observations. Depending upon the simulation set, they are less energetic by a factor of 2–7. This suggests that either something is missing in CCSN simulations or there are biases in our comparison. We identify several sources of bias for both the simulated and observed sets. In this preliminary analysis, we model some of these biases, but we recommend several ways to reduce the impact of these biases in the future. Given these biases, it is probably premature to make any conclusions about the fidelity of CCSN codes. Rather, the primary conclusion is that the current simulation and observational sets are inconsistent, all suffer from biases, and the path towards constraining CCSN theory requires careful consideration of the biases in both.

## ACKNOWLEDGEMENTS

The authors thank Ben Davies, Bernhard Müller, Hans-Thomas Janka, Ondrej Pejcha, Jose Prieto, Luc Dessart, and Dovi Poznanski for their careful scrutiny and thoughtful suggestions. This work has been assigned an LANL document release number LA-UR-19-23383.

## REFERENCES

- Arnett W. D., 1980, *ApJ*, 237, 541
- Benz W., Colgate S. A., Herant M., 1994, *Phys. D Nonlinear Phenom.*, 77, 305
- Bethe H. A., Wilson J. R., 1985, *ApJ*, 295, 14
- Bruenn S. W., Dirck C. J., Mezzacappa A., Hayes J. C., Blondin J. M., Hix W. R., Messer O. E. B., 2006, *J. Phys. Conf. Ser.*, 46, 393
- Bruenn S. W., Mezzacappa A., Hix W. R., Blondin J. M., Marronetti P., Messer O. E. B., Dirck C. J., Yoshida S., 2009, *J. Phys. Conf. Ser.*, 180, 012018
- Bruenn S. W. et al., 2013, *ApJ*, 767, L6
- Bruenn S. W. et al., 2016, *ApJ*, 818, 123
- Bruenn S. W. et al., 2018, preprint ([arXiv:1809.05608](https://arxiv.org/abs/1809.05608))
- Burrows A., Hayes J., Fryxell B. A., 1995, *ApJ*, 450, 830

- Burrows A., Radice D., Vartanyan D., 2019, *MNRAS*, 485, 3153
- Chugai N. N., Utrobin V. P., 2014, *Astron. Lett.*, 40, 291
- Colgate S. A., White R. H., 1966, *ApJ*, 143, 626
- Davies B., Beasor E. R., 2018, *MNRAS*, 474, 2116
- Davies B., Crowther P. A., Beasor E. R., 2018, *MNRAS*, 478, 3138
- Dessart L., Hillier D. J., 2019, *A&A*, 625, 7
- Díaz-Rodríguez M., Murphy J. W., Rubin D. A., Dolphin A. E., Williams B. F., Dalcanton J. J., 2018, *ApJ*, 861, 92
- Foreman-Mackey D., Hogg D. W., Lang D., Goodman J., 2013, *PASP*, 125, 306
- Goldberg J. A., Bildsten L., Paxton B., 2019, *ApJ*, 879, 20,
- Hamuy M., Pinto P. A., 2002, *ApJ*, 566, L63
- Hanke F., Marek A., Müller B., Janka H.-T., 2012, *ApJ*, 755, 138
- Herant M., Benz W., Hix W. R., Fryer C. L., Colgate S. A., 1994, *ApJ*, 435, 339
- Hillebrandt W., Mueller E., 1981, *A&A*, 103, 147
- Janka H.-T., Müller E., 1995, *ApJ*, 448, L109
- Kasen D., Woosley S. E., 2009, *ApJ*, 703, 2205
- Kuroda T., Takiwaki T., Kotake K., 2016, *ApJS*, 222, 20
- Lattimer J. M., Douglas Swesty F., 1991, *Nucl. Phys. A*, 535, 331
- Lentz E. J. et al., 2015, *ApJ*, 807, L31
- Liebrandt M., Whitehouse S. C., Fischer T., 2009, *ApJ*, 698, 1174
- Mabanta Q. A., Murphy J. W., 2018, *ApJ*, 856, 22
- Mazurek T. J., 1982, *ApJ*, 259, L13
- Melson T., Janka H. T., 2019, preprint ([arXiv:1904.01699](https://arxiv.org/abs/1904.01699))
- Melson T., Janka H.-T., Marek A., 2015a, *ApJ*, 801, L24
- Melson T., Janka H.-T., Bollig R., Hanke F., Marek A., Müller B., 2015b, *ApJ*, 808, L42
- Messer O. E. B., Bruenn S. W., Blondin J. M., Hix W. R., Mezzacappa A., Dirk C. J., 2007, *J. Phys. Conf. Ser.*, 78, 012049
- Messer O. E. B., Bruenn S. W., Blondin J. M., Hix W. R., Mezzacappa A., 2008, *J. Phys. Conf. Ser.*, 125, 012010
- Müller B., 2015, *MNRAS*, 453, 287
- Müller B., Melson T., Heger A., Janka H.-T., 2017a, *MNRAS*, 472, 491
- Müller T., Prieto J. L., Pejcha O., Clocchiatti A., 2017b, *ApJ*, 841, 127
- Müller B. et al., 2019, *MNRAS*, 484, 3307
- Murphy J. W., Burrows A., 2008, *ApJ*, 688, 1159
- Nakamura K., Takiwaki T., Kuroda T., Kotake K., 2015, *PASJ*, 67, 107
- O'Connor E. P., Couch S. M., 2018, *ApJ*, 854, 63
- Ott C. D., Roberts L. F., da Silva Schneider A., Fedrow J. M., Haas R., Schnetter E., 2018, *ApJ*, 855, L3
- Pejcha O., Prieto J. L., 2015, *ApJ*, 806, 225
- Popov D. V., 1993, *ApJ*, 414, 712
- Poznanski D., 2013, *MNRAS*, 436, 3224
- Radice D., Burrows A., Vartanyan D., Skinner M. A., Dolence J. C., 2017, *ApJ*, 850, 43
- Roberts L. F., Ott C. D., Haas R., O'Connor E. P., Diener P., Schnetter E., 2016, *ApJ*, 831, 12
- Skinner M. A., Dolence J. C., Burrows A., Radice D., Vartanyan D., 2018, *ApJS*, 241, 27
- Smartt S. J., 2015, *PASA*, 32, e016
- Smith N., Li W., Filippenko A. V., Chornock R., 2011, *MNRAS*, 412, 1522
- Steiner A. W., Hempel M., Fischer T., 2013, *ApJ*, 774, 17
- Sukhbold T., Ertl T., Woosley S. E., Brown J. M., Janka H.-T., 2016, *ApJ*, 821, 38
- Summa A., Hanke F., Janka H.-T., Melson T., Marek A., Müller B., 2016, *ApJ*, 825, 6
- Vartanyan D., Burrows A., Radice D., Skinner M. A., Dolence J., 2018, *MNRAS*, 477, 3091
- Vartanyan D., Burrows A., Radice D., Skinner M. A., Dolence J., 2019, *MNRAS*, 482, 351
- Williams B. F., Hillis T. J., Murphy J. W., Gilbert K., Dalcanton J. J., Dolphin A. E., 2018, *ApJ*, 860, 10,
- Wilson J. R., 1985, in Centrella J., Leblanc J., Bowers R. L., eds, *Numerical Astrophysics*. Jones & Bartlett, Boston, p. 422
- Woosley S. E., Heger A., Weaver T. A., 2002, *Rev. Mod. Phys.*, 74, 1015
- Woosley S. E., Heger A., 2007, *Phys. Rep.*, 442, 269

This paper has been typeset from a  $\text{\LaTeX}$  file prepared by the author.